Fabrication of a microfluidic device by using two-photon lithography on a positive photoresist

van der Velden, Gijs; Fan, D.; Staufer, U.

DOI
10.1016/j.mne.2020.100054

Publication date
2020

Document Version
Final published version

Published in
Micro and Nano Engineering

Micro and Nano Engineering 7 (2020) 100054

Contents lists available at ScienceDirect

Micro and Nano Engineering

journal homepage: www.journals.elsevier.com/micro-and-nano-engineering

Research paper

Fabrication of a microfluidic device by using two-photon lithography on a positive photoresist

G. van der Velden, D. Fan, U. Staufer*

Department of Precision and Microsystems Engineering, Faculty of Mechanical Engineering, Delft University of Technology, Mekelweg 2, 2628 CD Delft, the Netherlands

ARTICLE INFO

Keywords:
Two-photon lithography
Positive photoresist
Voxel shape
Microfluidic channel
Organ-on-Chip

ABSTRACT

Organ-on-chip (OoC) technology is increasingly used for biomedical research and to speed up the process of bringing a drug from lab to the market. The main fluidic components of an OoC device are microfluidic channels and porous membranes arranged in three dimensions. Current chips are often assembled from several parts. In the development phase a small change in design will cause a delay in the research because a new prototype has to be built and assembled again step-by-step. The research discussed in this paper addresses this point by targeting a monolithic 3D device that can be fabricated in a single lithography and development step, enabling rapid prototyping. Two-photon lithography (TPL) was used in combination with a positive photoresist AZ 4562. The exposure process was characterized, which included an experimental and theoretical study of the voxel size and shape. It was found that the voxel has an hourglass-shape for the laser power settings that were required for process stability. The smallest pores we could produce with these settings measured 250 nm in diameter. The TPL process was then used to fabricate a microfluidic device featuring two crossed channels each one on a separate height-level, connected by a membrane in the centre. Access to the channels was provided through 4 reservoirs from the top-side of the device. The device was successfully filled with water and dried to see whether it can withstand the corresponding capillary forces.

1. Introduction

The time for a newly developed biomedical drug to reach the market is long [1]. Currently this process takes ten to twelve years, which is mainly due to the length of the testing phase [2]. Substances are tested in vitro, by plain cell-culture experiments and in vivo, i.e. in animals before clinical testing can start. The main advantage of current in vitro tests is its high-throughput by simultaneously operating many devices in parallel. Organ-on-chip (OoC) technology shares this advantage, but in addition it produces more relevant results, as it offers the possibility to simulate essential physiological aspects of the organ or tissue [3], i.e. it is closer to in vivo testing. Besides having ethical issues, in vivo animal testing is time consuming and expensive [4]. OoC technology addresses also these points, because it offers a significant reduction in the number of animal tests. After animal testing, additional tests have to be conducted using human tissue before entering clinical trials [5]. These tests could also be reduced when using OoC devices.

Microfluidic channels and porous membranes are the main components of an OoC device [6]. In academic research, channels are typically fabricated in-house by moulding their shapes into polydimethylsiloxane (PDMS), while the membranes are usually purchased from commercial sources and assembled [7]. Assembling and stretching flimsy membranes can be time consuming and it is challenging to achieve good leak-tight sealings to the channels. Bilayer fabrication approaches using standard photolithography have been used to produce channels and membranes based on both a chemically amplified resist (EPR) [8] as well as SU-8 [9]. In both cases the UV absorption sensitivity of different layers were adjusted to achieve selectivity, meaning that more complicated multilayer structures would need increasingly complex process optimization. A monolithic fabrication process, which allows fabricating relatively large channels and porous membranes at different height levels and in one process would be attractive and come with the advantage of rapid prototyping. Stereo-lithography is one suitable process, albeit with a resolution limit of ~25 μm [10].

Here we propose such a technique, which is based on two-photon lithography (TPL). TPL is a direct laser writing method, which is currently used in many micro fabrication applications [11–15]. It exploits the fact that a two-photon process non-linearly depends on the light intensity [11]. The required intensity is only achieved in a small volume around the focal point of the laser, called the voxel [12]. The laser can be focused within the photosensitive resin, and by moving the voxel, three dimensional structures can be created. In earlier research, TPL is

* Corresponding author.
E-mail address: u.staufer@tudelft.nl (U. Staufer).

https://doi.org/10.1016/j.mne.2020.100054
Received 30 October 2019; Received in revised form 14 April 2020

almost always used in combination with a negative photoresist, which is then called two-photon polymerization (2PP) [16]. The shape of voxel in that case is found to be ellipsoidal. Hence, the maximum diameter of the voxel is found at the height of the focal plane, i.e. at $z = 0$ [12,13].

Using 2PP with negative-tone photoresist for additively fabricating channels in a piece of bulk would significantly increase the processing time [17]. Subtractive fabrication of channels and pores in negative photoresist using femtosecond laser ablation via 3-photon absorption has been demonstrated, although the process is slow as the 3-photon process requires slow scan speeds to achieve the necessary light intensity [18]. Microfluidic structures have also been written in a positive-tone chemically amplified resist using 2PP with a custom tailored photoacid generator [19]. Instead, we used TPL with AZ 4562, a commercially available positive photoresist. This allowed fast production of a complete microfluidic device featuring two channels crossing each other at different height and being separated by a membrane, in one lithography and development step. In future the technique would also permit one-step fabrication of integrated devices within microfluidic channels, such as filters, traps, pumps, lenses, gratings, and so on [20,21].

2. Theory

TPL makes use of the two-photon absorption (TPA) of a photosensitive molecule. AZ 4562 consists of Novolac as backbone polymer and diazonaphtoquinone (DNQ) as photosensitive molecule [22]. The main function of DNQ is an inhibitor to the dissolution of the surrounding Novolac. During exposure the DNQ is functionalized with carboxylic acid groups (COOH). The COOH-groups make the DNQ more soluble and easily removed when immersed in a caustic-water developer solution. Once the DNQ is removed, the surrounding resin will also be dissolved in the solution.

The process of TPL on a positive photoresist can be described by Eq. (1). Here M is the unexposed DNQ, M^* is the excited DNQ and P is the relative amount of DNQ that reacted and was functionalized with a COOH-group.

$$M \underset{k_2}{\overset{k_1}{\leftrightarrow}} M^* \overset{k_3}{\rightarrow} P \tag{1}$$

It is well known that the amount of excited DNQ quickly reaches equilibrium [23]. Therefore the second rate equation can be well approximated by $\frac{dM^*}{dt} = 0$, which is used to solve the rate equations to obtain Eq. (2).

$$M = M_0 exp\left(\frac{-k_1 k_3}{k_2 + k_3} t_I\right). \tag{2}$$

M_0 is the initial amount of DNQ present in the resist, k_1 is the rate at which M is excited, k_2 is the rate at which the excited DNQ molecules fall back to the initial state and k_3 is the rate constant describing the transition from the excited DNQ to the product, functionalized with a COOH-group. Finally t_I is the interaction time between the laser and the photoresist.

The rate equations and the interaction time are described by Cao et al. [14], who also used these relations to obtain a final expression describing the voxel diameter $d(z)$ at distance z from the focal plane. This equation is given in Eq. (3). In the original paper by Cao et al., it was only used to determine the voxel width at $z = 0$. Here, we also use it to define the entire voxel shape.

$$d(z) = w(z)\sqrt{ln\left(\frac{4C\eta^2 P_{laser}^2 t}{f\tau(\pi h\nu w^2(z))^2 ln\frac{M_0}{M_{th}}}\right)}. \tag{3}$$

In Eq. (3), η is the transmittance of optical system, P_{laser} is the laser power, t is the exposure time during the process, f and τ are the repetition rate and the pulse width of the laser respectively, h is Planck's constant, ν is the light frequency and M_{th} is the material threshold value for the dissolvable amount of DNQ. The beam radius $w(z)$ at distance z from the focal plane is described by Eq. (4), where w_0 is the beam waist radius and f_L the Rayleigh length [15]. Finally C is a material constant related to TPA, described by Eq. (5). Here Φ is the quantum efficiency, δ the TPA cross-section, A_E is Einstein's coefficient of spontaneous emission and C_0 is a material constant.

$$w(z) = w_0\sqrt{1 + \left(\frac{z}{f_L}\right)^2}. \tag{4}$$

$$C = \frac{\Phi\delta C_0}{A_E + C_0}. \tag{5}$$

The voxel height can be expressed as $2z_{max}$, where z_{max} is the distance from the focal plane to where $d(z) = 0$.

To simplify the modelling and fit the equation to the obtained data, the constant C, the exposure time t and the material threshold value M_{th} were combined into a variable K_{CtM}, given in Eq. 6. The other fitting variable is the beam waist radius w_0.

$$K_{CtM} = \frac{Ct}{ln\left(\frac{M_0}{M_{th}}\right)}. \tag{6}$$

3. Methods and experiments

A 10 μm thick layer of AZ 4562 (Microchemicals GmbH, Ulm, Germany) was spincoated on a 170 μm thick glass slide (Menzel-Gläser, Bad Wildungen, Germany). After spin-coating, a soft-bake at 110 °C for 5 min was performed on a hotplate. Finally, before exposure the sample was hydrated in air for 15 min. The specimen was exposed using TPL (Photonic Professional GT, Nanoscribe, Germany) via an objective lens (magnification 63×, numerical aperture 1.4). A femtosecond erbium-doped fibre laser (Toptica Photonics AG, Munich, Germany) with a mean laser power of 50 mW, a second harmonic wavelength of 780 nm, 80 MHz repetition rate and a pulse width of 100 fs was used. During the exposure series, the laser power was gradually increased from 0.5 to 5 mW while the scanning speed was varied between 10 and 100 μm/s in order to study the dose dependence. After exposure the sample was developed in AZ 400 K developer (Microchemicals GmbH) diluted with deionized water in a ratio of 1:4.

The pores were fabricated by vertically scanning a single voxel through the resist. For evaluating the voxel height and shape, the voxel was lowered into the resist in steps of 50 nm, starting 0.5–1 μm above the surface of the resist. This value depended on the tilt of the sample. After edge bead removal and tilt correction there was still a tilt between 0 and 0.25°. The lowering of the focal point into the resist is illustrated in Fig. 1.

For the manufacturing of the channels, multiples of 10 μm thick resist layers were spin coated on top of each other, up to a total thickness of 50 μm. The exposure of the channels was performed with 10 mW laser power and a scanning speed of 20 mm/s. This increased the processing speed at the expense of resolution. The channels were developed for 80 min, during which the developer solution was stirred with a magnetic stirrer (IKA Labortechnik RH basic, IKA-Werke GmbH, Staufen, Germany).

For the measurement of the pores, the sample was sputter coated

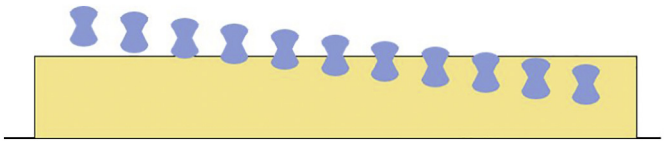

Fig. 1. The voxel was lowered into the resist in steps of 50 nm.

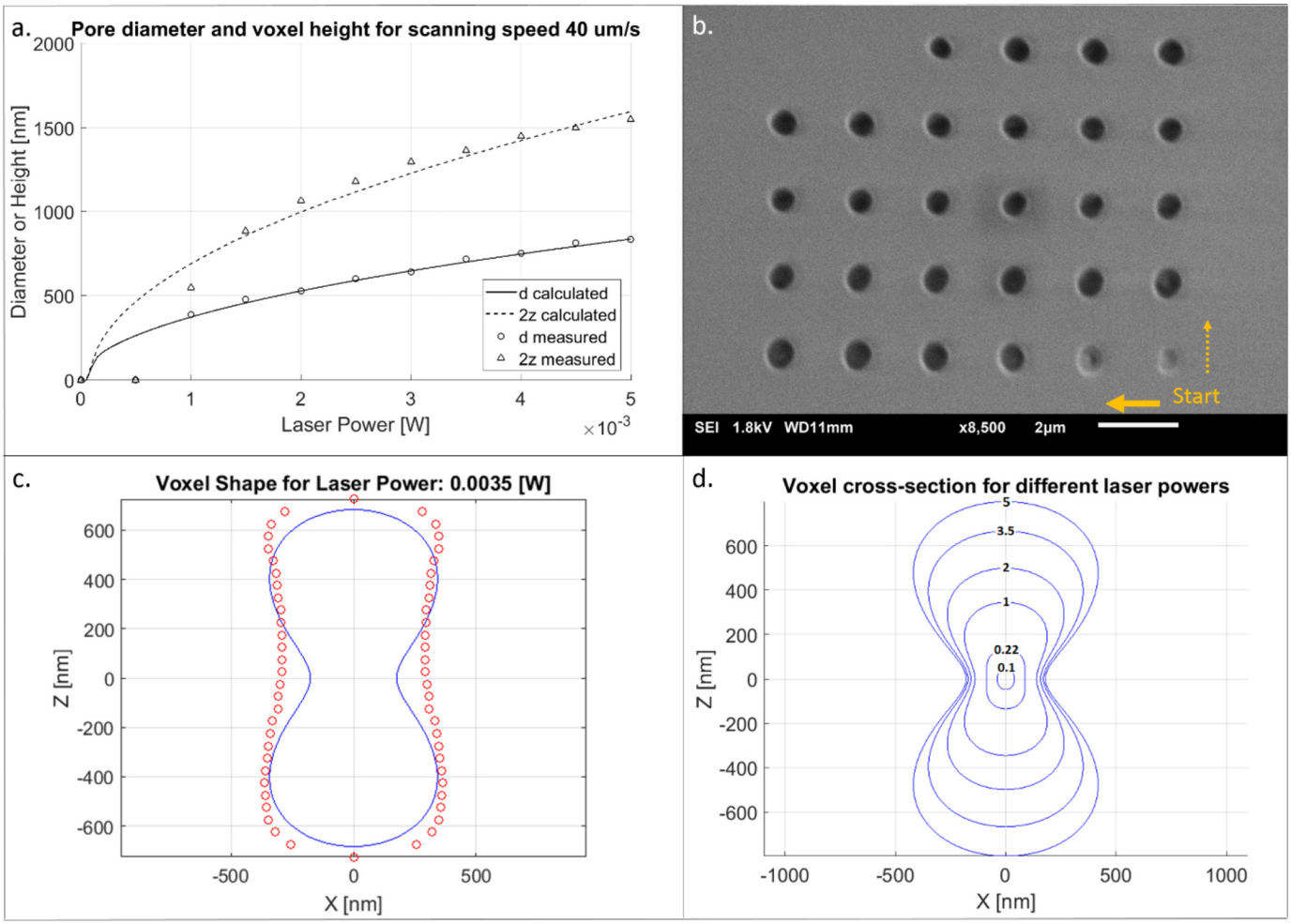

Fig. 2. a) Model fit to the measurements. The circles indicate the voxel diameter and the triangles indicate the voxel height, which is twice the distance z from the focal plane. b) Micrograph of the voxel diameter and height test by lowering the voxel with steps of 50 nm, from right to left, starting in the lower right corner and then rastering upwards. The scanning speed was 40 µm/s and the laser power was 3.5 mW. c) The 2D model of the voxel shows an hourglass-like shape. The measured data is added with red circles. The diameter is smaller at the waist, i.e. where z = 0. The maximum diameter lies at z = 550 nm in the measurements and at z = 450 in the model. d) The cross-section of the voxel changes with laser power. As the laser power increases, the voxel takes a more hourglass-like shape. The laser power is indicated in mW for each profile. (For interpretation of the references to colour in this figure legend, the reader is referred to the web version of this article.)

(SC7620, Quorum Technologies, Lewes, UK) with gold or gold/palladium layers with a thickness of around 5 nm. The coated sample was imaged in a scanning electron microscope (SEM, Jeol JSM-6010LA, Tokyo, Japan) and the measurements were done with the SEM software and a custom-made MATLAB script. The channels were also imaged with an optical microscope (Keyence Digital Microscope VHX-6000, Osaka, Japan), and a white light interferometer (Bruker). Finally, the channels were filled with water via capillary action and dried under optical microscope to observe liquid flow and structural integrity of the channels.

4. Results and discussion

The data obtained from the voxel diameter and height experiments was combined in a model where the main equation Eq. (3) was fitted for K_{CtM} and w_0. The average result of three individual measurements for a scanning speed of 40 µm/s is shown in Fig. 2a. The fitting values found were $K_{CtM} = 2.75 \times 10^{-60}$ m^4s^2 and $w_0 = 125.14$ nm. For a laser power of 1 mW and higher, the experimental data and the theory correspond well. Hence, these values can be used for predicting the voxel dimensions and as input for designing 3D structures. Similar curves were found for experiments at scanning speeds between 10 and 100 µm/s. The fitted values for the beam waist radius were between 119.45 nm and 127.13 nm, with an average of 123.79 nm. The fitted values for K_{CtM} decreased linearly with decreasing scanning speed as expected from Eq. (6).

The value found for w_0 was slightly smaller than the one expected from literature [13]. A cause of this difference could be the refractive index of the photoresist. The w_0 value for AZ 4562 was estimated based on the paper by Cao et al. who used the similar photoresist AZ P4620 [14]. If the actual refractive index would be lower than assumed, a smaller beam waist radius would be expected. Other causes for a different beam waist radius could be most likely overdevelopment, lens aberrations, or systematic errors in the optical path of the laser. Small fluctuations in the laser power could explain the variation in the values obtained for w_0.

The exposed voxel that was lowered step-by-step into the resist is shown in Fig. 2b. The laser power was 3.5 mW and the scanning speed 40 µm/s. It can be observed that the diameter of the pores in row 3, columns 4 and 5, is smaller than the diameter of the surrounding pores. This indicates where the laser is focused at the height of the surface of the resist. When the laser is focused above or below the surface, the diameter of the pores increases at first, then decreases and abruptly stops. This measurement demonstrates that if the laser intensity away from the focal plane is still high enough to initiate two photon processes, TPA is initiated in a larger cross-sectional area than at the waist

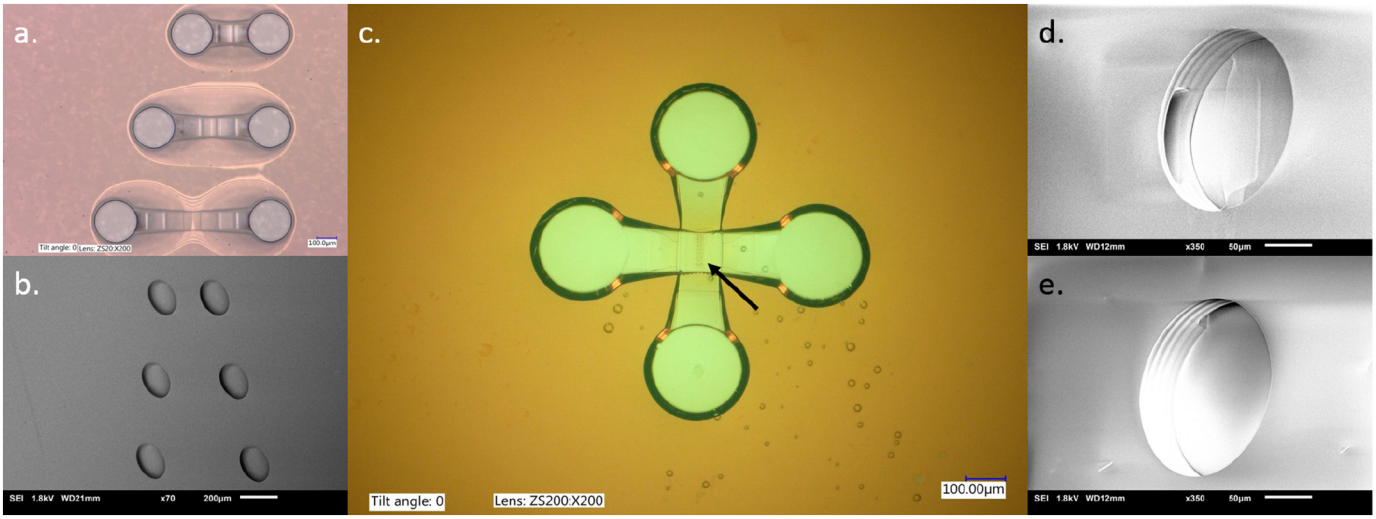

Fig. 3. a) Optical image of three fully developed channels with a width of 100 µm and a length of respectively 180, 380 and 580 µm. The scale bar measures 100 µm. b) SEM micrograph of the same channels imaged under a tilt-angle of 45°. The scale bar measures 200 µm. c) Optical image of a fully developed microfluidic device with two perpendicular channels at different heights in the resist with a porous membrane of thickness 10 µm at their intersection (arrow). The width of the channels is 100 µm and the height is 10 µm. The inlet and outlet holes have a diameter of 210 µm. d) SEM micrograph under a 45° angle of an in- or outlet hole for the higher channel (from left to right in c). The scale bar measures 50 µm. e) SEM micrograph of an in- or outlet hole for the lower channel (from top to bottom in c). The scale bar measures 50 µm.

of the beam. Consequently a larger amount of material is removed during the development process. For modelling the pore diameter, this would mean that the maximum voxel diameter instead of the diameter at $z = 0$ must be considered.

The found fitting parameters were used to calculate the voxel diameter as function of the distance z from the focal plane. The result of the calculation for the case of a laser power of 3.5 mW is shown in Fig. 2c. It can be observed that the shape partially follows the profile of the Gaussian laser beam and, hence, has an hourglass-like shape. The dots display the measured voxel diameter and height as obtained from Fig. 2b. The measured voxel dimensions also show the hourglass shape. The actual diameter at the beam waist is larger than the modelled one. This could be caused by diffusion of the functionalized DNQ into the unexposed material. There will be more diffusion near the waist of the beam than at the distance z where the maximum diameter is found, because the DNQ will diffuse in all directions. Another cause of the size difference could again be aberrations in the optical system, or, most likely over-development. The actual voxel height is slightly higher than calculated. Also here, over-development could explain this deviation. In addition we have to consider that, the datapoints for a diameter of 0 are drawn 50 nm above and below the voxel. In reality the real voxel top and bottom can be anywhere within this extra step of 50 nm.

The shape of the voxel strongly depends on the laser power. The positive resist has a very low threshold value and the laser is operated at low power. The predicted cross-section of the voxel for laser powers between 0.1 and 5 mW is shown in Fig. 2d. The first laser power for which the maximum voxel diameter occurs at $z = 0$, shows a voxel with a cigar shape. As the laser power gets even lower, the expected shape will look like an ellipsoid again. The same argument holds for constant laser power but reduced sensitivity of the resist for two photon processes.

4.1. Pores and channels

The smallest pores that were produced were around 250 nm in diameter. They were produced with a scanning speed of 30 µm/s and a laser power of 0.5 mW. This laser power did not initiate TPA for a scanning speed of 40 µm/s, which is due to the related shorter exposure time. A lower scanning speed corresponds to a longer exposure time.

In theory it should be possible to produce pores with a diameter smaller than 250 nm. However, the experiments showed that for AZ 4562, TPA is initiated at very low laser powers. At such low laser powers shot noise can come into play, which could become the limiting factor. A solution could be to use a positive-tone resist with a lower refractive index and higher threshold intensity for TPA. Finally dark erosion is an important factor for the size limitations. The developer also attacks unexposed resist [24], which in our case is very critical as we need long exposure times for fully developing the long channels.

Channels of different sizes were produced, each with two access-holes of 210 µm diameter reaching all the way to the glass-substrate. Fig. 3a shows an optical microscope image of the channels, which can be seen through the transparent resist. The halo-like feature encircling the structure is most likely due to under etching from the access-holes during the development. An SEM micrograph of the same channels is shown in Fig. 3b, proving that the channels are buried inside the resist. Finally, the one-step monolithic microfluidic device consisting of two perpendicular channels at different heights separated by a membrane was produced. An optical image of this device is shown in Fig. 3c. The length of the channels is 350 µm and they are separated by a membrane 10 µm in height. At the intersection of the channels the pores of the membrane are visible. The micrographs in Fig. 3d and 3e show a zoom-in picture of access-holes, which have a height of 50 µm. The entrance to the channels is visible in the left rim (Fig. 3d), and top rim (Fig. 3e) respectively. Due to dark erosion during the development process, the channels are wider at the entrance to the holes as seen in Fig. 3c. After filling the device with water, the drying process was observed (see Video S1 in supplementary information), showing the flow of liquid inside the channels and structural integrity of the channels and membrane after drying.

5. Summary and conclusions

A new method was used for a single step fabrication of a microfluidic device that consists of two channels and a separating membrane. Two-photon lithography was used on a positive-tone photoresist AZ 4562. Pore characterization showed that when the light intensity is high enough to also initiate two-photon absorption further away from the focal plane, the voxel shape follows the Gaussian beam profile and takes an hourglass shape. The maximum voxel diameter, and therefore pore diameter is not found at the focal point of the laser, but at a

distance z from the focal plane. Experiments showed that the voxel indeed takes the hourglass shape. Therefore, for the fabrication of high-resolution pores, the maximum voxel diameter has to be taken into account during the writing procedure. The smallest pores created were 250 nm. Due to the long development times, dark erosion, which is also location dependent, must be taken into account when designing critical dimensions. The channels in the fabricated microfluidic device have a width of 100 µm, a height of 10 µm and a length of 350 µm. The channels are separated in height by 10 µm. Atomic layer deposition of silica could be used in future to render the 3D polymer structure more robust and chemically inert as previously demonstrated by M. Hermatschweiler et al. [25] for a photonic band-gap structure.

Supplementary data to this article can be found online at https://doi.org/10.1016/j.mne.2020.100054.

Credit author statement

G. van der Velden did the design of the device, conducted most of the lab work and data analyses, and wrote the first draft of the manuscript. D. Fan introduced and supervised TPL activities, helped with lab work, suggested technology improvements, revised the manuscript. U. Staufer initiated the project and concept, supervised the activities and advised on experiments, technology improvements and data representation. All authors discussed the results, and jointly revised the final manuscript and approved it.

Declaration of Competing Interest

The authors declare having no conflict of interest.

Acknowledgements

We thank R. Pleeging for valuable discussions and R. Luttjeboer for his support in the laboratory. This research did not receive any specific grant from funding agencies in the public, commercial, or not-for-profit sectors.

References

[1] I. Torjesen, Drug development: the journey of a medicine from lab to shelf, Pharm. J. 12 (2015) 1–7.
[2] J. Endres, The drug development process: From the lab to your medicine cabinet, (2017) https://www.gopraxis.com/the-drug-development-process-from-the-lab-to-your-medicine-cabinet/ , Accessed date: 25 February 2020.
[3] S.N. Bhatia, D.E. Ingber, Microfluidic organs-on-chips, Nat. Biotechnol. 32 (2014) 760–772, https://doi.org/10.1038/nbt.2989.
[4] K. Groff, E. Bachli, M. Lansdowne, T. Capaldo, Review of evidence of environmental impacts of animal research and testing, Environments. 1 (2014) 14–30, https://doi.org/10.3390/environments1010014.
[5] T. Capaldo, Animal Data Is Not Reliable for Human Health Research, https://www.livescience.com/46147-animal-data-unreliable-for-humans.html, (2014) , Accessed date: 25 February 2020.
[6] N.S. Bhise, J. Ribas, V. Manoharan, Y.S. Zhang, A. Polini, S. Massa, M.R. Dokmeci, A. Khademhosseini, Organ-on-a-chip platforms for studying drug delivery systems, J. Control. Release 190 (2014) 82–93, https://doi.org/10.1016/j.jconrel.2014.05.004.
[7] T. Pasman, D. Grijpma, D. Stamatialis, A. Poot, Flat and microstructured polymeric membranes in organs-on-chips, J. R. Soc. Interface 15 (2018) 20180351, https://doi.org/10.1098/rsif.2018.0351.
[8] M. Kitsara, M. Chatzichristidi, D. Niakoula, D. Goustouridis, K. Beltsios, P. Argitis, I. Raptis, Layer-by-layer UV micromachining methodology of epoxy resist embedded microchannels, Microelectron. Eng. 83 (2006) 1298–1301, https://doi.org/10.1016/j.mee.2006.01.157.
[9] Y. Moser, R. Forti, S. Jiguet, T. Lehnert, M.A.M. Gijs, Suspended SU-8 structures for monolithic microfluidic channels, Microfluid. Nanofluid. 10 (2011) 219–224, https://doi.org/10.1007/s10404-010-0657-5.
[10] Y. Zhou, The recent development and applications of fluidic channels by 3D printing, J. Biomed. Sci. 24 (2017) 80, https://doi.org/10.1186/s12929-017-0384-2.
[11] L. Li, J.T. Fourkas, Multiphoton polymerization, Mater. Today 10 (2007) 30–37, https://doi.org/10.1016/S1369-7021(07)70130-X.
[12] S. Maruo, O. Nakamura, S. Kawata, Three-dimensional microfabrication with two-photon-absorbed photopolymerization, Opt. Lett. 22 (1997) 132, https://doi.org/10.1364/OL.22.000132.
[13] X. Zhou, Y. Hou, J. Lin, A review on the processing accuracy of two-photon polymerization, AIP Adv. 5 (2015) 030701, , https://doi.org/10.1063/1.4916886.
[14] H.-Z. Cao, M.-L. Zheng, X.-Z. Dong, F. Jin, Z.-S. Zhao, X.-M. Duan, Two-photon nanolithography of positive photoresist thin film with ultrafast laser direct writing, Appl. Phys. Lett. 102 (2013) 201108, https://doi.org/10.1063/1.4807678.
[15] G. Williams, M. Hunt, B. Boehm, A. May, M. Taverne, D. Ho, S. Giblin, D. Read, J. Rarity, R. Allenspach, S. Ladak, Two-photon lithography for 3D magnetic nanostructure fabrication, Nano Res. 11 (2018) 845–854, https://doi.org/10.1007/s12274-017-1694-0.
[16] L. Li, M. Hong, M. Schmidt, M. Zhong, A. Malshe, B. Huis, V. Kovalenko, Laser nano-manufacturing – state of the art and challenges, CIRP Ann. 60 (2011) 735–755, https://doi.org/10.1016/j.cirp.2011.05.005.
[17] E. Montinaro, M. Grisi, M.C. Letizia, L. Pethö, M.A.M. Gijs, R. Guidetti, J. Michler, J. Brugger, G. Boero, 3D printed microchannels for sub-nL NMR spectroscopy, PLoS One 13 (2018) e0192780, , https://doi.org/10.1371/journal.pone.0192780.
[18] W. Xiong, Y.S. Zhou, X.N. He, Y. Gao, M. Mahjouri-Samani, L. Jiang, T. Baldacchini, Y.F. Lu, Simultaneous additive and subtractive three-dimensional nanofabrication using integrated two-photon polymerization and multiphoton ablation, Light Sci Appl. 1 (2012) e6, https://doi.org/10.1038/lsa.2012.6.
[19] W. Zhou, An efficient two-photon-generated Photoacid applied to positive-tone 3D microfabrication, Science 296 (2002) 1106–1109, https://doi.org/10.1126/science.296.5570.1106.
[20] K. Sugioka, Y. Cheng, Femtosecond laser three-dimensional micro- and nanofabrication, Appl. Phys. Rev. 1 (2014) 041303, , https://doi.org/10.1063/1.4904320.
[21] M. Nouri-Goushki, A. Sharma, L. Sasso, S. Zhang, B.C.J. Van der Eerden, U. Staufer, L.E. Fratila-Apachitei, A.A. Zadpoor, Submicron patterns-on-a-Chip: fabrication of a microfluidic device incorporating 3D printed surface ornaments, ACS Biomater. Sci. Eng. 5 (2019) 6127–6136, https://doi.org/10.1021/acsbiomaterials.9b01155.
[22] M. Campbell, D.N. Sharp, M.T. Harrison, R.G. Denning, A.J. Turberfield, Fabrication of photonic crystals for the visible spectrum by holographic lithography, Nature. 404 (2000) 53–56, https://doi.org/10.1038/35003523.
[23] J. Albers, Intensity dependence of photochemical reaction rates for photoresists, J. Electrochem. Soc. 127 (1980) 1400, https://doi.org/10.1149/1.2129906.
[24] MicroChemicals, Basic Chemistry of Developers, https://www.microchemicals.com/downloads/application_notes.html, (2020) , Accessed date: 25 February 2020.
[25] M. Hermatschweiler, A. Ledermann, G.A. Ozin, M. Wegener, G. von Freymann, Fabrication of silicon inverse woodpile photonic crystals, Adv. Funct. Mater. 17 (2007) 2273–2277, https://doi.org/10.1002/adfm.200601074.